Exposing binding-favourable facets of perovskites for tandem solar cells

Junke Wang[1,†]*, Shuaifeng Hu[1,†], Zehua Chen[2,†], Zhongcheng Yuan[1], Pei Zhao[1,3], Akash Dasgupta[1], Fengning Yang[1], Jin Yao[4], Minh Anh Truong[5], Gunnar Kusch[6], Esther Y-H. Hung[1], Nick R. M. Schipper[7], Laura Bellini[7], Guus J. W. Aalbers[7], Zonghao Liu[8,9], Rachel A. Oliver[6], Atsushi Wakamiya[5], René A.J. Janssen[7], and Henry J. Snaith[1]*

[1]Clarendon Laboratory, Department of Physics, University of Oxford, Parks Road, Oxford OX1 3PU, United Kingdom

[2]Beijing Computational Science Research Center, Beijing 100193, China

[3]Research Center for Computational Science, Institute for Molecular Science, Okazaki 444-8585, Japan

[4]National Thin Film Cluster Facility for Advanced Functional Materials, Department of Physics, University of Oxford, Parks Road, Oxford OX1 3PU, United Kingdom

[5]Institute for Chemical Research, Kyoto University, Gokasho, Uji, Kyoto 611-0011, Japan

[6]Department of Materials Science and Metallurgy, University of Cambridge, Cambridge, United Kingdom

[7]Molecular Materials and Nanosystems and Institute for Complex Molecular Systems, Eindhoven University of Technology, P.O. Box 513, 5600 MB, Eindhoven, The Netherlands

[8]Wuhan National Laboratory for Optoelectronics, Huazhong University of Science and Technology (HUST), Wuhan, China

[9]Hubei Optics Valley Laboratory, Wuhan, China

*Email: junke.wang@physics.ox.ac.uk; henry.snaith@physics.ox.ac.uk

[†]These authors contributed equally

DFT calculations

Surface energies are calculated using the crystal cleaving and surface relaxation method[1,2], following

$E_{surf}(t)=E_{cl}+E_{rel}(t)$, (1)

where E_{cl} is the crystal-cleaving energy, and $E_{rel}(t)$ is the energy gain due to the surface relaxation of the slab with termination t.

Here, the crystal-cleaving energy E_{cl} is defined as

$E_{cl}=\left[E_{slab}^{unrel}(t_1)+E_{slab}^{unrel}(t_2)-nE_{bulk}\right]/4S$, (2)

where $E_{slab}^{unrel}(t_1)$ and $E_{slab}^{unrel}(t_2)$ are the total energies of unrelaxed t_1-terminated and t_2-terminated slab pairs, respectively. In this work, we have considered three cases (t_1, t_2) = (FABr, $PbBr_2$), (t_1, t_2) = (Br_2, FAPbBr), and (t_1, t_2) = ($FABr_3$, Pb), respectively. E_{bulk} is the bulk energy per formula unit in the cubic $FAPbBr_3$, n is the total number of bulk formula units in the two slabs, 1/4 means the four surfaces in total are created upon crystal cleavage when considering two slabs, and S refers to the area of the surface.

Since both sides of the slab are allowed to relax, the relaxation energy E_{rel} for each of the surfaces can be obtained by

$E_{rel}(t)=\left[E_{slab}^{rel}(t)-E_{slab}^{unrel}(t)\right]/2S$, (3)

where $E_{slab}^{rel}(t)$ is the t -terminated slab energy after structural relaxation.

In the presence of the PEA or 4-F-PEA cation, we additionally consider following reactions with enthalpy ΔH,

$R-FA+mPEABr \rightarrow R-PEA+mFABr(\Delta H)$, (4)

and

$R-FA+m(4-F-PEABr) \rightarrow R-(4-F-PEA)+mFABr(\Delta H)$, (5)

where R represents the slab. $R-FA$, $R-PEA$, and $R-(4-F-PEA)$ are notations for the FA, PEA, or 4-F-PEA cation binding at the slab surface. m is the number of ligands replaced in the reaction. The corresponding reaction enthalpy is then defined as

$\Delta H = E(R-PEA) + m\,E(FABr) - E(R-FA) - m\,E(PEABr)$, (6)

and

$\Delta H = E(R-(4-F-PEA)) + m\,E(FABr) - E(R-FA) - m\,E(4-F-PEABr)$, (7)

where $E(¿)$ refers to the total energies of the corresponding configurations.

Taking the chemical reactions into account, the surface energy of the slab with the addition of PEA or 4-F-PEA cation is then given by $E'_{surf}(t) = ¿\ E_{surf}(t) + \Delta H/2S$.

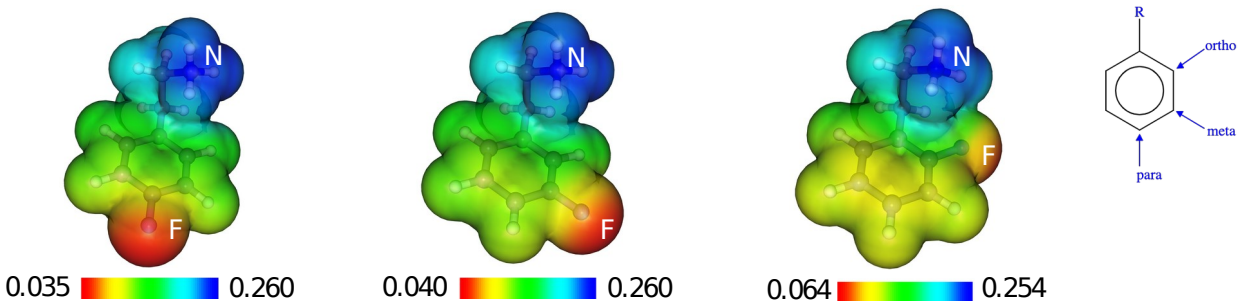

Supplementary Figure 1. PEA cations. Calculated electrostatic potentials (a.u.) of pFPEA, mFPEA, and oFPEA cations. The dipole moment of pFPEA (4-F-PEA) is larger compared to other cations (mFPEA, oFPEA, PEA, and FA). We anticipate that this larger dipole moment will lead to stronger interactions with perovskite precursors and reduced crystallographic disorder[3]. We also note that all PEA derivatives exhibit a higher dipole moment than FA, suggesting more favourable interactions with lead halide species.

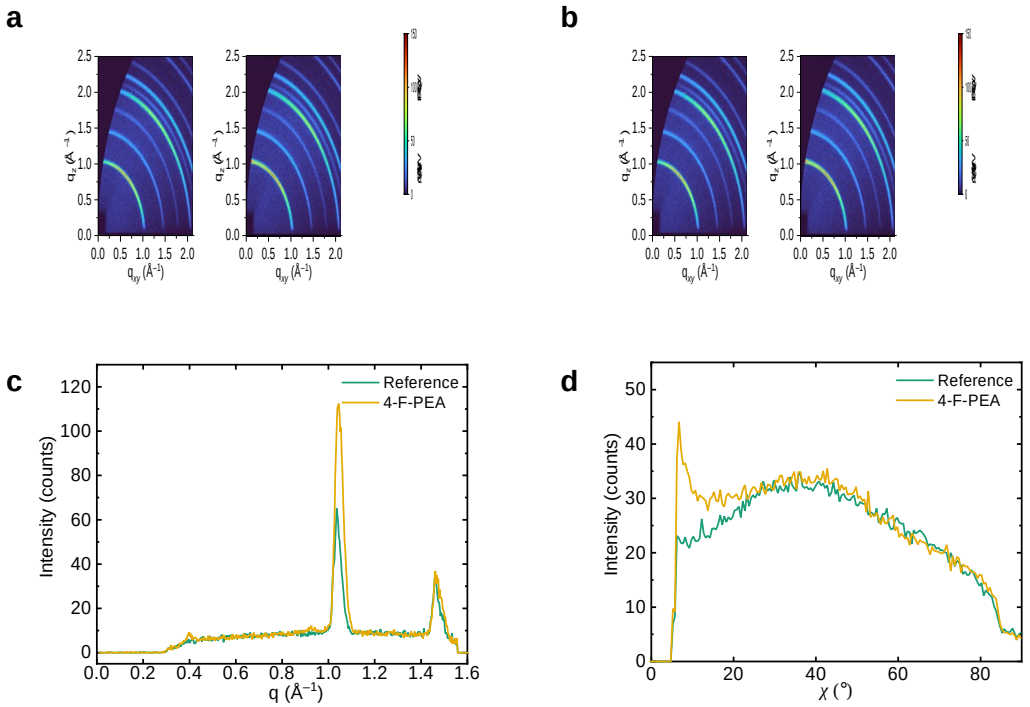

Supplementary Figure 2. Crystallinity of perovskite films. a,**b**, GIWAXS patterns of the reference film $Cs_{0.2}FA_{0.8}Pb(I_{0.6}Br_{0.4})_3$ (**a**) and the film with the addition of 5 mol% 4-F-PEACl (**b**). **c**, Out-of-plane line profiles obtained by integrating sectors at χ = 0 to 20°. **d**, Azimuthal integration of the (100) peak at χ = 0 to 90°.

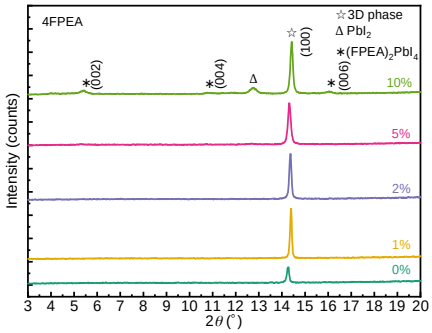

Supplementary Figure 3. Crystal structure of 4-F-PEA added wide-bandgap perovskites. The zoomed-in XRD patterns of wide-bandgap perovskite thin films at varying 4-F-PEA concentrations (0–10 mol%). Asterisk: n = 1 2D phase; Triangle: PbI_2 phase; Star: 3D phase. For the perovskite film containing 10 mol% 4-F-PEA, we assign the peaks at 5.4°, 10.8°, and 16.4° to the (002), (004), and (006) crystallographic planes of the n = 1 phase (4-F-PEA_2PbI_4), respectively. As mentioned in our Methods section, we incorporated an equal molar amount of 4-F-PEA to replace FAI. When only the n = 1 phase is formed, 4-F-PEA reacts with PbI_2 in a 2:1 ratio, leaving a small amount of unreacted PbI_2 in the film. This is consistent with the PbI_2 phase observed in the XRD pattern. We also note a slight decrease in the lattice parameter for films with 1 and 2 mol% 4-F-PEA (**Fig. 1f**), which can be attributed to the introduction of the smaller Cl anion into the perovskite structure (4-F-PEACl), while 4-F-PEA cation does not incorporate to the crystal lattice. At 5 mol%, we expect that a small amount of the larger 4-F-PEA cation may incorporate into the crystal and/or distort the octahedral structure, resulting in a lattice expansion. By the time we reach 10 mol%, phase separation between the 3D and 2D structures begins to occur; the majority of 4-F-PEA forms n = 1 phases, while the increased Cl content further contracts the crystal lattice.

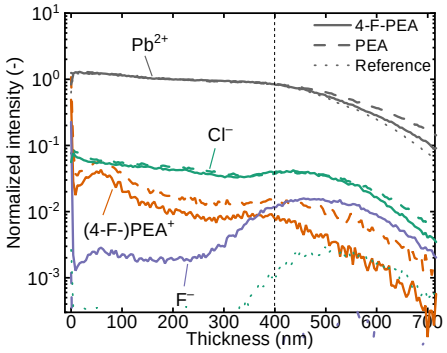

Supplementary Figure 4. Composition profile of perovskite films. Depth profile of $Cs_{0.2}FA_{0.8}Pb(I_{0.6}Br_{0.4})_3$ films (reference) with 1 mol% of PEACl and 4-F-PEACl treatment. The dashed line is an indication of the perovskite/HTL interface. The sputtering time is normalised to the thickness of perovskite films (~400 nm) estimated from the cross-sectional SEM image. In the initial experiments, Me-4PACz was used instead of MPA-CPA as the HTL and an equivalent mole of $PbCl_2$ was added together with PEACl and 4-F-PEACl. We note that compared to the cations, the Cl anion is uniformly distributed through the perovskite films.

Supplementary Figure 5. Termination-dependent surface states and ligand passivation. a, Localised charge density (yellow cloud) due to the presence of the Br_{Pb}^{3-} antisite defect at the FABr (100) and $PbBr_2$ (100) surfaces. Orange, Br; Grey, Pb; Light blue, N; Brown, C; Light red, H. **b**, Charge transfer after passivation by PEA^+ and EDA^{2+} on both surfaces, where the yellow (blue) cloud refers to accumulation (depletion) of the local charge density. Atomic structures without clouds are shown in **Supplementary Fig. 7**.

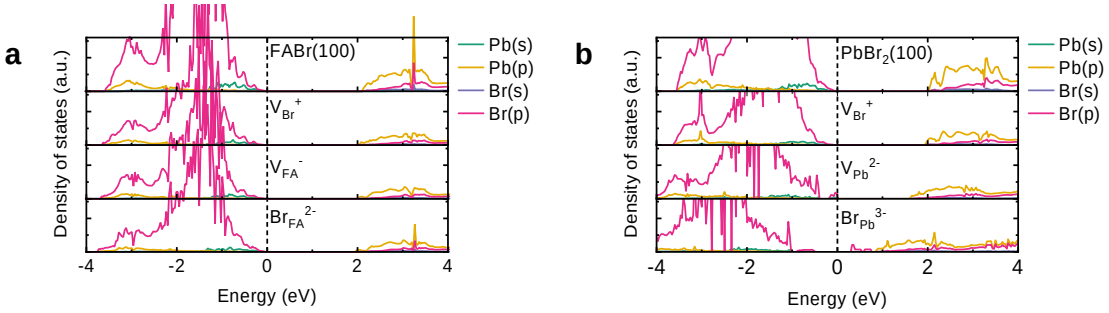

Supplementary Figure 6. Termination-dependent surface states induced by defects. Calculated projected density of states (PDOS) for FABr (100) (**a**) and $PbBr_2$ (100) (**b**) surfaces after introducing V_{Br}^{+}, V_{FA}^{-}, Br_{FA}^{2-}, and V_{Pb}^{2-} defects. Top, pristine surface.

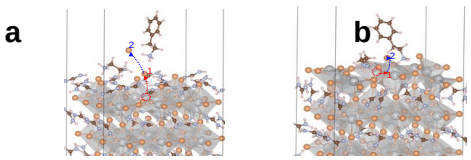

Supplementary Figure 7. Ligand passivation process. The local structure of FABr (100) and $PbBr_2$ (100) surfaces with Br_{Pb}^{3-} antisite defects after PEA^+ and EDA^{2+} passivation. Orange, Br; Grey, Pb; Light blue, N; Brown, C; Light red, H. The antisite Br anion (dotted red circle) moves to position “1” of the outmost atomic layer and kicks out the Br anion at this position to position “2”. The migration paths are indicated by dotted lines.

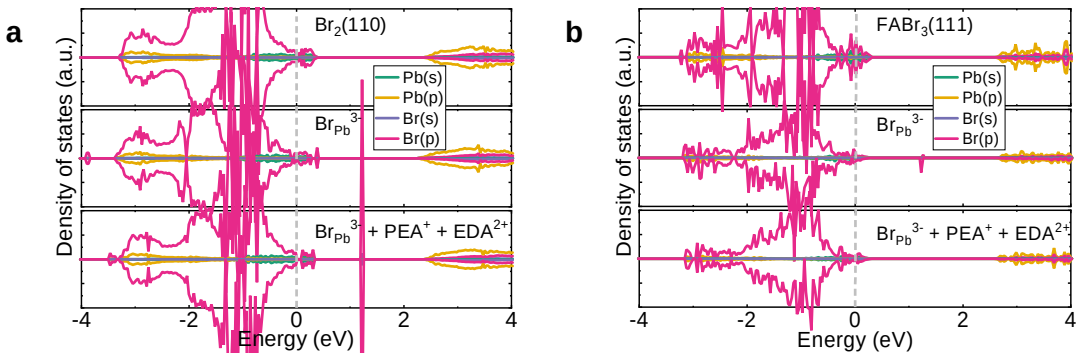

Supplementary Figure 8. Termination-dependent passivation for wide-bandgap perovskite interface. a,**b**, Calculated projected density of states (PDOS) for Br_2 (110) (**a**) and $FABr_3$ (111) (**b**) surfaces. Top, pristine surface; Middle, surface with a Br_{Pb}^{3-} antisite defect; Bottom, surface passivated by PEA^+ and EDA^{2+} cations. States related to organic molecules are not shown as they have low contributions near the band edges. The Fermi energy level is set to zero.

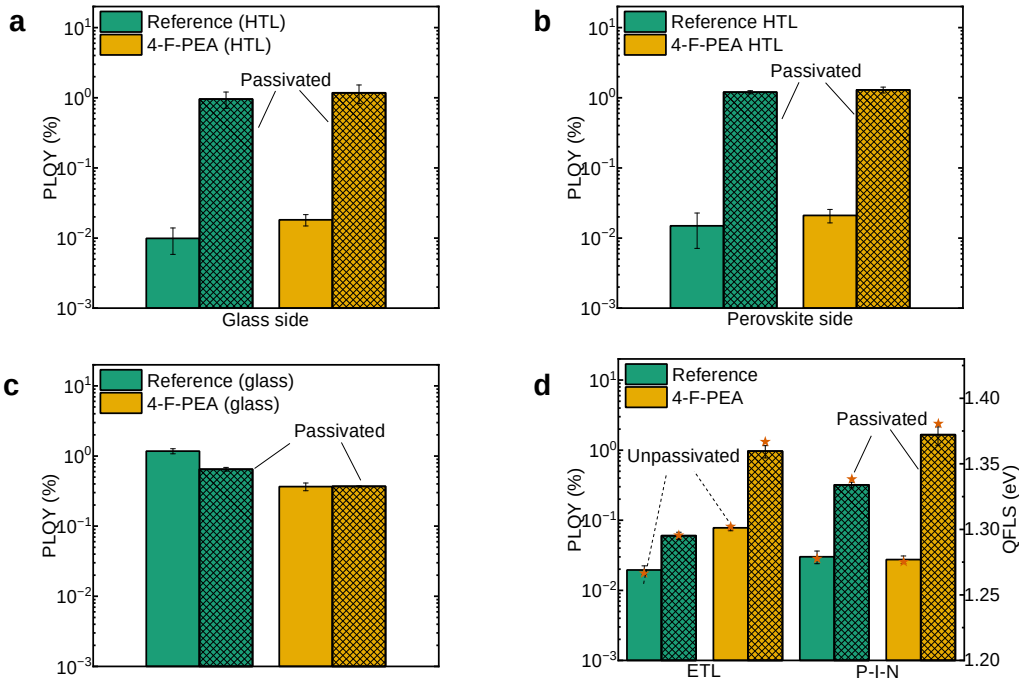

Supplementary Figure 9. Optical property of wide-bandgap perovskite films. **a**,**b**,**c**, PLQY of reference and 4-F-PEA (1 mol%) wide-bandgap perovskite films processed on glass/ITO/HTL measured from the glass (**a**) and perovskite top side (**b**), and on bare glass substrates (**c**). The samples shown in **Supplementary Fig. 9a–c** and **Fig. 2d** were fabricated in the same batch. **d**, PLQY of wide-bandgap perovskites processed on glass and covered by an ETL (ETL stack) and in a p-i-n stack, these samples were prepared in a different batch than shown in **Fig. 2d** to show the reproducibility of the trend. Samples with PEA/EDA surface passivation are displayed with cross-hatched patterns.

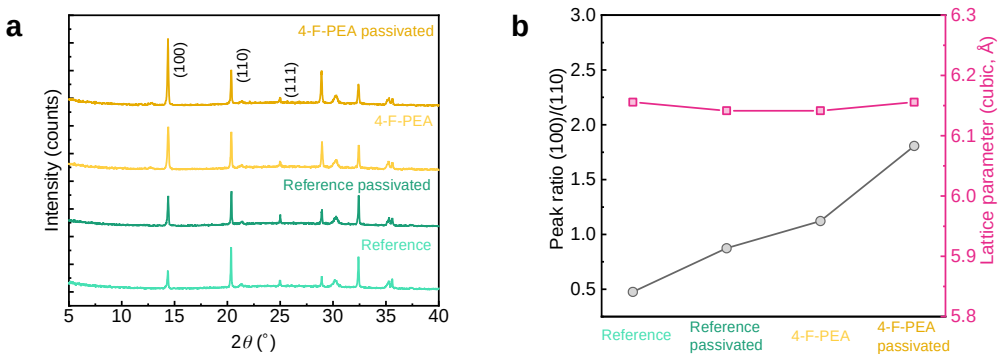

Supplementary Figure 10. Crystal structure of wide-bandgap perovskites before and after surface treatment. **a**, XRD patterns and **b**, cubic lattice parameters of reference and 1 mol% 4-F-PEA-added perovskite thin films deposited on glass/ITO/HTL before and after surface treatment. Interestingly, we find that the (100)/(110) peak ratios slightly increase after the surface treatment for both samples. This can be attributed to a recrystallisation effect that occurs during the post-treatment, which somehow reorients the perovskite towards a more thermodynamically favourable facet (**Fig. 1d**). Based on the PLQY data (**Supplementary Fig. 9a–b**), we infer that these post-treatments globally enhance crystal quality of the films, thus also contributing to the mitigated non-radiative recombination losses at the buried interface. We consider that an enhanced (100) orientation may also positively affect the HTL interface, although this effect appears to be saturated, as comparable PLQY values are observed for both the reference/passivated and 4-F-PEA/passivated samples deposited on the HTL. This interesting additional finding further verifies our claim that a more (100)-oriented perovskite presents inherently less defect density.

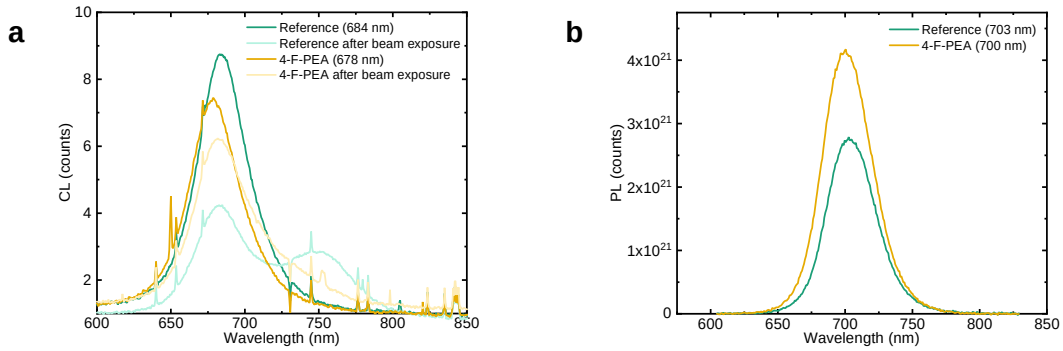

Supplementary Figure 11. Emission properties of perovskite films. Mean CL spectra of reference and 4-F-PEA-added (1 mol%) perovskite films before and after e-beam induced phase separation (**a**). We note that compared with the PL spectra (**b**), the peak position of the CL spectra is slightly blue-shifted. This can be attributed to reduced reabsorption caused by a smaller carrier-generation volume produced by e-beam excitation[4]. Furthermore, the addition of a small amount of Cl (4-F-PEACl) also induced a minor blue shift in the emission spectra.

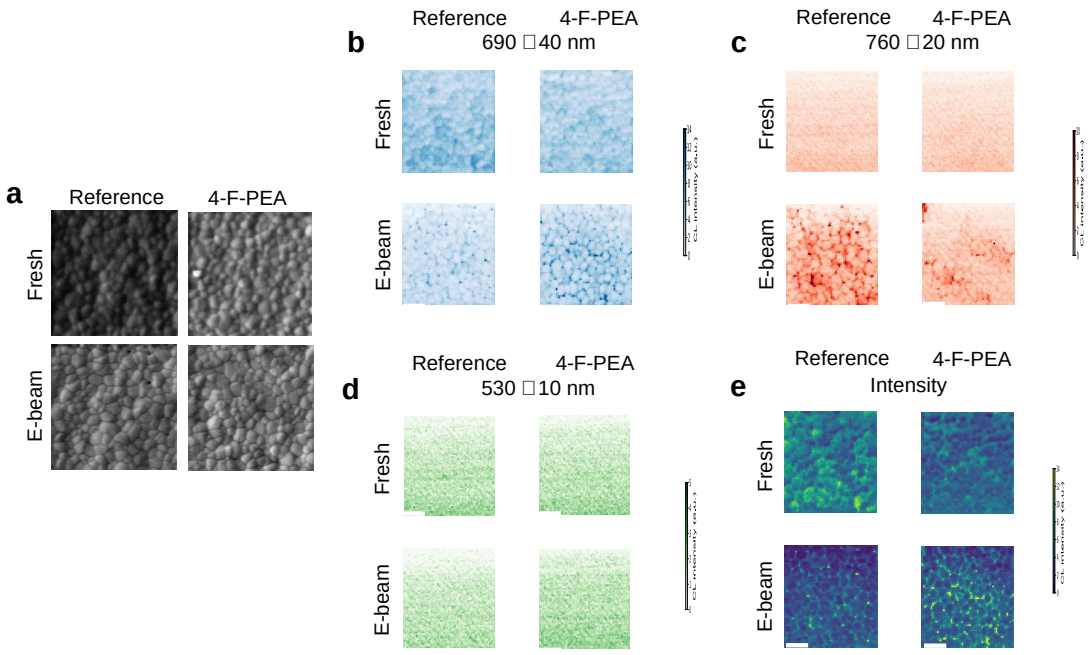

Supplementary Figure 12. Nanoscale optical properties of wide-bandgap perovskite films. a, Top-view SEM images of reference and 4-F-PEA (1 mol%) perovskite films with and without e-beam-induced phase separation. **b–d**, CL maps with 690 ± 40 nm, 760 ± 20 nm, and 530 ± 10 nm filters to acquire emissions from the original and segregated (I-rich) perovskite phases, and PbI_2 phases, respectively. **e**, CL intensity (panchromatic) mapping. The scale bars are 500 nm.

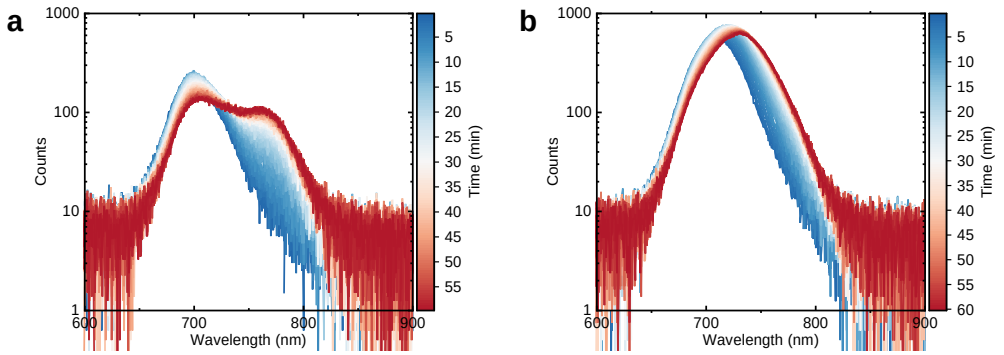

Supplementary Figure 13. Phase stability. Time-dependent PL spectra of reference (**a**) and 4-F-PEA (**b**) perovskite films under 1-sun equivalent illumination using 530 nm laser. The PL spectra were collected every 30 s during a 60 min tracking period. A more rapid light-induced phase separation is seen in the reference sample (**a**) compared to the 4-F-PEA sample (**b**). This is consistent with the CL data (**Supplementary Fig. 11**), suggesting enhanced phase stability after the modification.

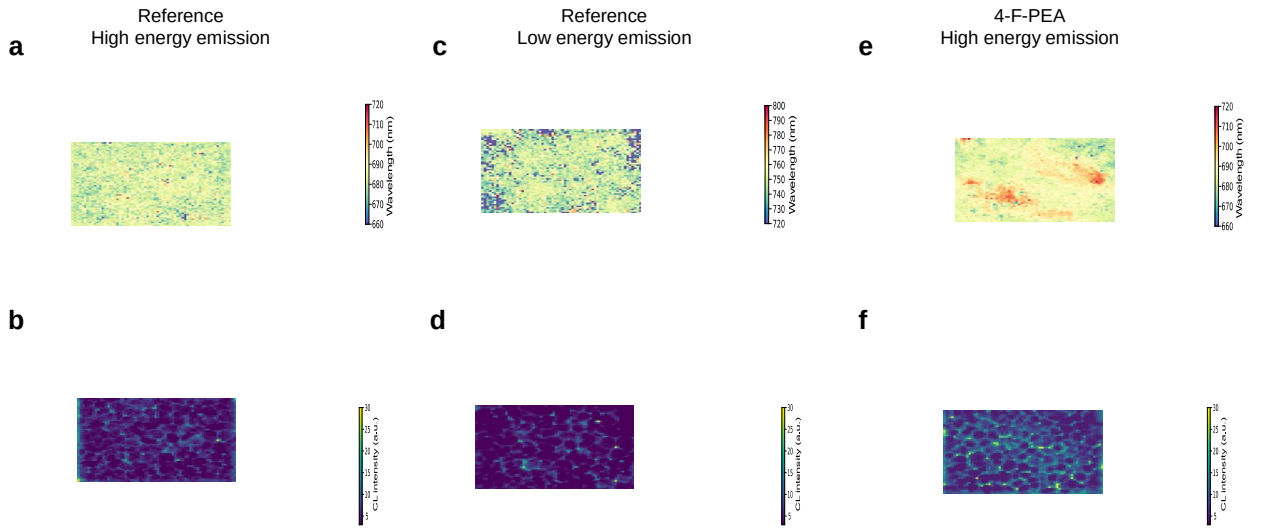

Supplementary Figure 14. Nanoscale phase heterogeneity of perovskite films after e-beam exposure. a,**b**, Hyperspectral (**a**) and CL intensity images (**b**) of the reference film with a spectral window of 660–720 nm (high energy). The mean emission wavelength is 683.1 ± 5.2 nm. **c**,**d**, Hyperspectral (**c**) and CL intensity images (**d**) of the reference film with a spectral window of 720–800 nm (low energy). The mean emission wavelength is 746.6 ± 11.6 nm. **e**,**f**, Hyperspectral (**e**) and CL intensity images (**f**) of the 4-F-PEA film with a spectral window of 660–720 nm (high energy). The mean emission wavelength is 685.5 ± 6.2 nm. The scale bars are 500 nm.

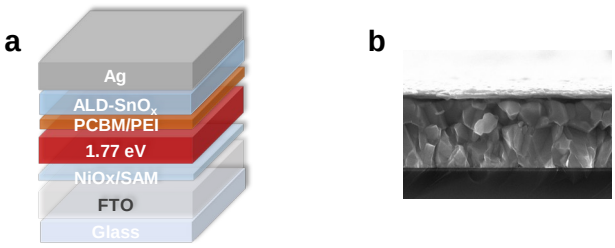

Supplementary Figure 15. Single-junction wide-bandgap PSCs. a,**b**, Device layout (**a**) and cross-sectional SEM image of single-junction p-i-n wide-bandgap PSCs. The scale bar is 500 nm.

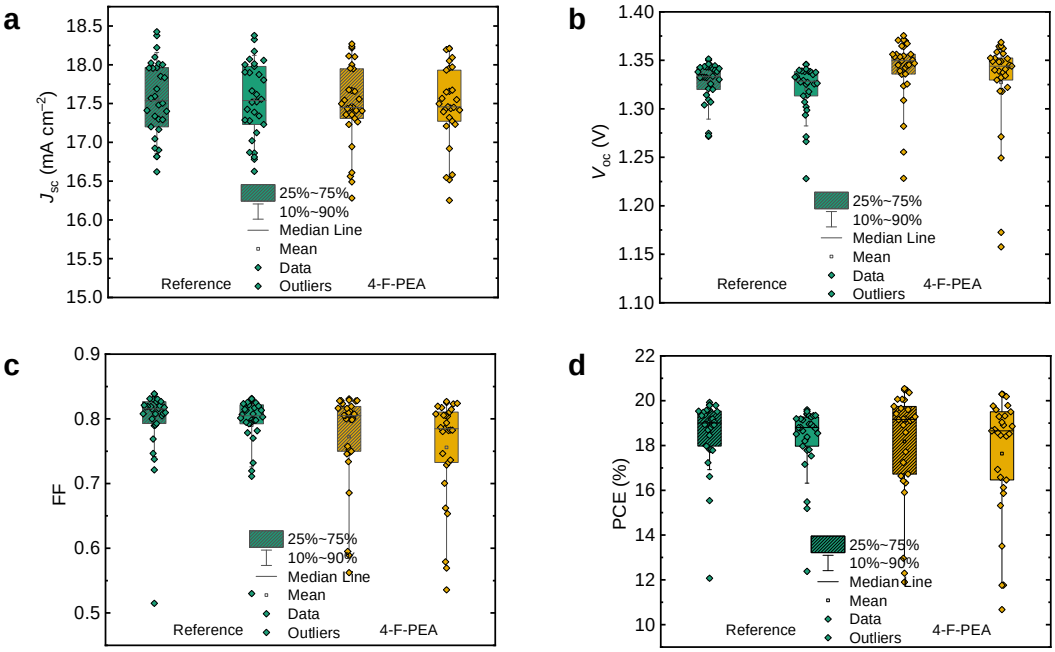

Supplementary Figure 16. Photovoltaic performance of wide-bandgap PSCs. PV parameters (reverse scans, left; forward scans, right) of reference and 4-F-PEA (1 mol%) devices. For each variation, 30 devices from 3 different batches are shown. In the boxplots, the mean (open square), median (centre line), 25th and 75th percentiles (box limits), minimum (–) and maximum (+), outliers (△), and 10th and 90th percentiles (whiskers) are shown.

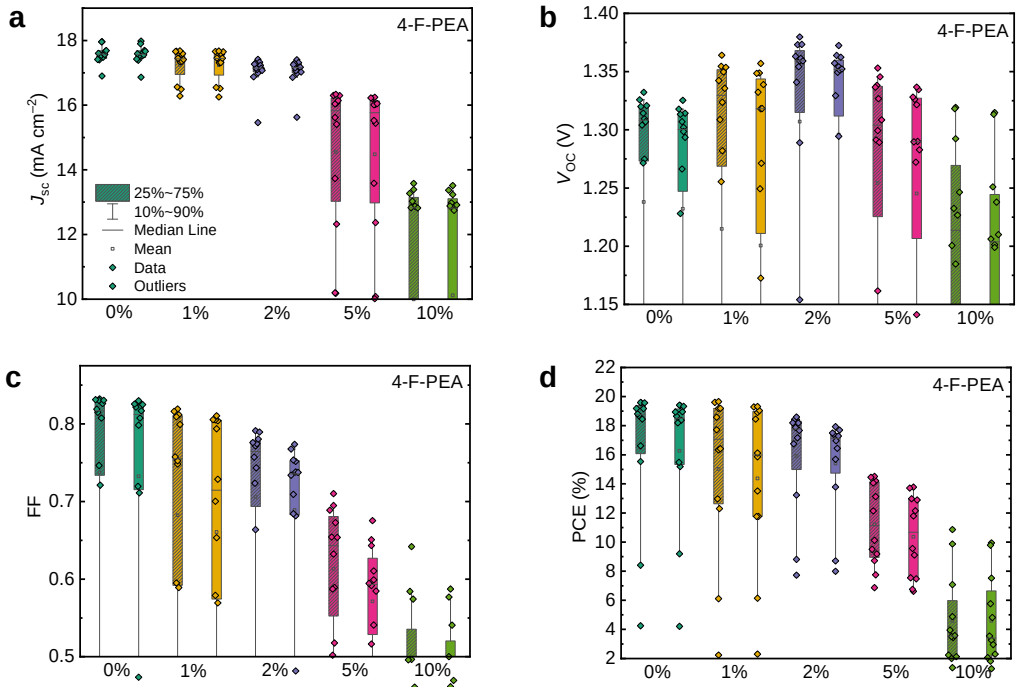

Supplementary Figure 17. Photovoltaic performance of wide-bandgap single-junction PSCs. PV parameters (reverse scans, left; forward scans, right) of reference and 4-F-PEA (1–10 mol%) devices. For each variation, 12 devices from the same batch are shown. In the boxplots, the mean (open square), median (centre line), 25th and 75th percentiles (box limits), minimum (–) and maximum (+), outliers (△), and 10th and 90th percentiles (whiskers) are shown. In our initial device optimisation, we found that adding 4-F-PEA at concentrations of 1–2 mol% can positively increase the V_{OC} of 1.77 eV PSCs. This is crucial for improving the overall performance of tandem solar cells. However, as the concentration of 4FPEA increases to 5–10%, we observe a gradual decrease in all cell parameters. This can be attributed to increased shunt losses in the solar cells, which stem from higher film roughness at increased additive concentrations. Additionally, the formation of thicker low mobility species, such as 2D phases and/or insulating organic layers, can hinder charge collection. This particularly impacts the J_{SC} and FF, despite the increase in the PLQY and implied V_{OC} values[5].

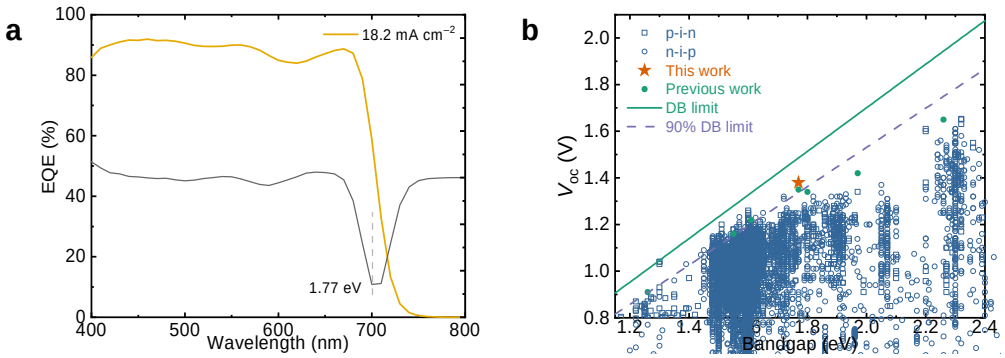

Supplementary Figure 18. EQE spectrum and bandgap-dependent V_{OC} for p–i–n single-junction PSCs. a, The EQE and its first derivative as a function of photo energy for single-junction wide-bandgap PSCs. **b**, The cell data were acquired from an open-access perovskite database[6]. In the plot, the DB (detailed balance) limit (solid line), 90% of the DB limit (dashed line), the highest V_{OC} of this work (solid star) and open-source data (open brackets) are shown. Data from our recent multijunction work is shown as green solid dots[7].

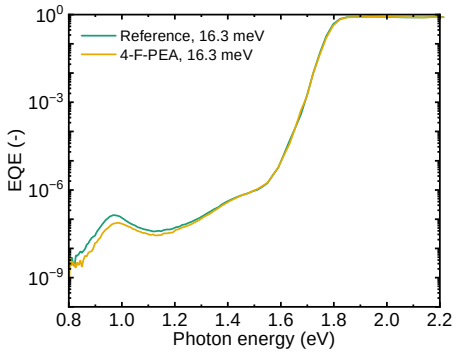

Supplementary Figure 19. EQE spectrum. Semilogarithmic plot of the sensitive EQE spectrum of reference and 4-F-PEA devices. This was measured using a sensitive EQE setup using a lock-in-amplifier. The Urbach energy is calculated to be 16.3 meV for both devices.

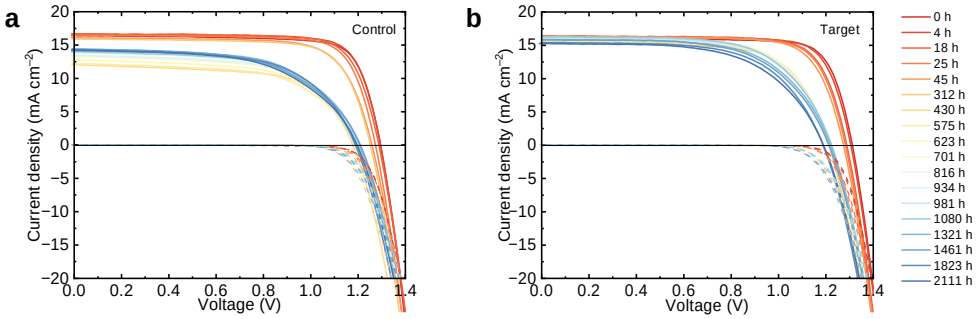

Supplementary Figure 20. Photovoltaic performance of wide-bandgap PSCs during ageing. Dark and light (AM1.5G) *J*–*V* characteristics of single-junction wide-bandgap PSCs measured (in the ambient) after storing in N_2 in an 85 °C ageing chamber.

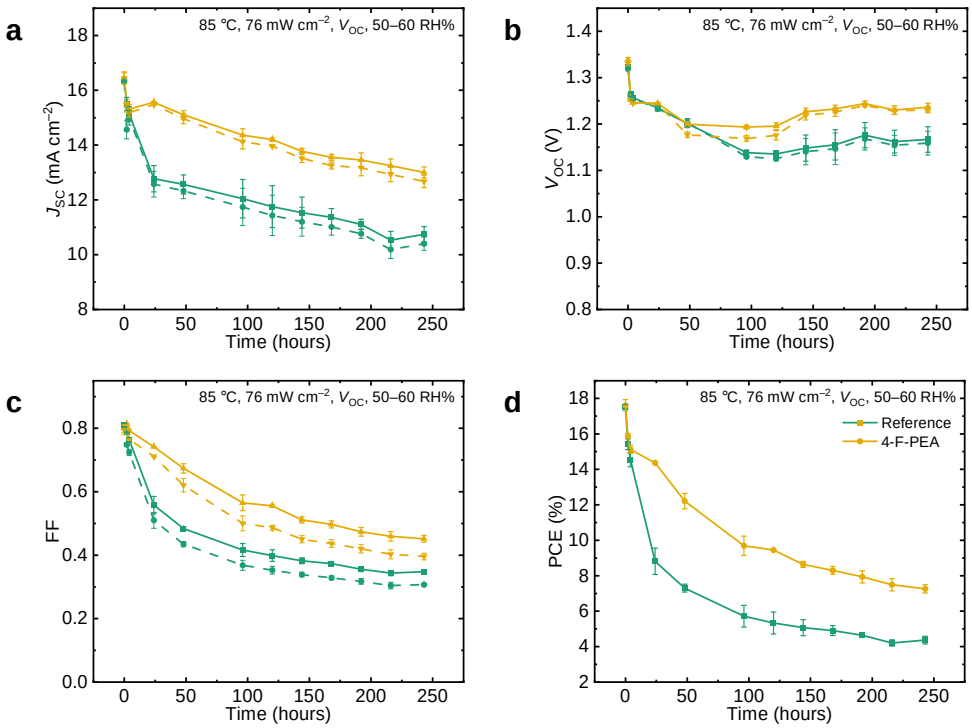

Supplementary Figure 21. Photovoltaic performance of wide-bandgap PSCs during ageing. The PV parameters of **a**, J_{SC}, **b**, V_{OC}, **c**, FF, and **d**, PCE (MPP efficiency) of encapsulated solar cells measured after storing at 85 °C in ambient under full-spectrum simulated sunlight (~76 mW cm^{-2}). The solid lines are data points from reverse scans while the dashed lines are from the forward scans. The RH is a measure of the room of the ageing box.

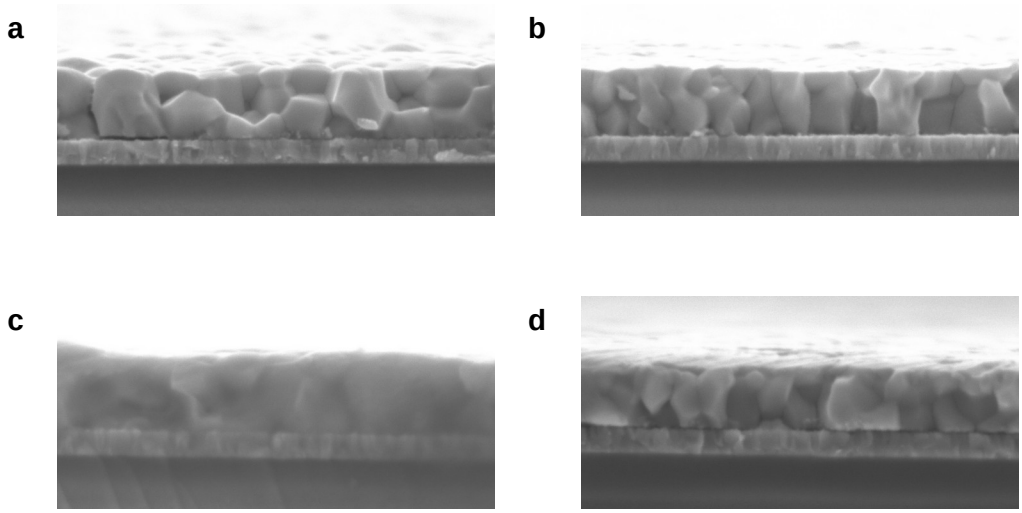

Supplementary Figure 22. Morphology of wide-bandgap perovskites after ageing. a–**d**, Cross-sectional SEM images of reference (**a**,**c**) and 4-F-PEA (**b**,**d**) perovskite before ageing (**a**,**b**) and after storing at 85 °C in ambient (50–60 RH%) under full-spectrum simulated sunlight (~76 mW cm^{-2}) for more than 240 hours. Note that the top ETL and metal contact were delaminated from the perovskite layer after removing the encapsulation glass on top. The scale bars are 500 nm.

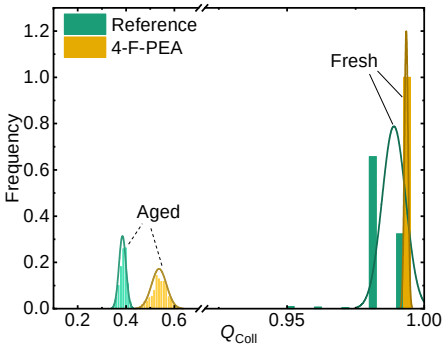

Supplementary Figure 23. Stability of wide-bandgap PSCs. Histograms of the charge collection quality (Q_{coll}, by comparing the QFLS measured at the device OC and SC, Fig. 3d) for reference and 4-F-PEA devices, measured after 0 h (fresh) and 2100 h of 85 °C dark ageing in N_2. Interestingly, we find that the Q_{Coll} distribution in the aged 4-F-PEA device is slightly broader than that of the reference. We hypothesise that the main degradation pathways are located near the perovskite/charge-transporting layer interfaces, which hinder charge collection quality and consequently affect the J_{SC} and FF values (**Supplementary Fig. 20**). For the reference device, we anticipate a more rapid decay at both the HTL and ETL interfaces, creating barriers for charge extraction. For the 4-F-PEA device, the better-passivated top surface may preserve some percolation pathways for charge-carrier extraction. While it would be interesting to investigate whether Q_{Coll} could converge after even longer ageing tests, we believe it is justified to conclude that the material modification enhances thermal stability.

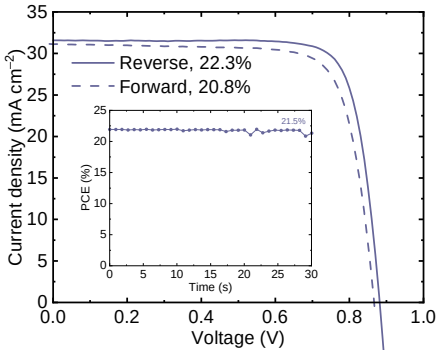

Supplementary Figure 24. Photovoltaic performance of narrow-bandgap single-junction solar cell. The *J*–*V* characteristics of champion tandem solar cells measured with an aperture area of 0.25 cm^2. The inset shows the PCE after 30 s of MPPT.

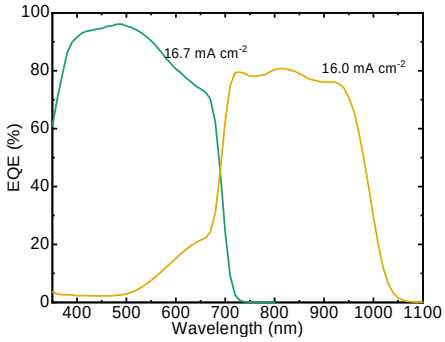

Supplementary Figure 25. EQE response. The EQE spectra of wide- and narrow-bandgap sub-cells in all-perovskite tandem solar cells. The J_{SC} was obtained by integrating with the AM 1.5G spectrum. The calculated mismatch factor for the current-limiting junction is 0.994.

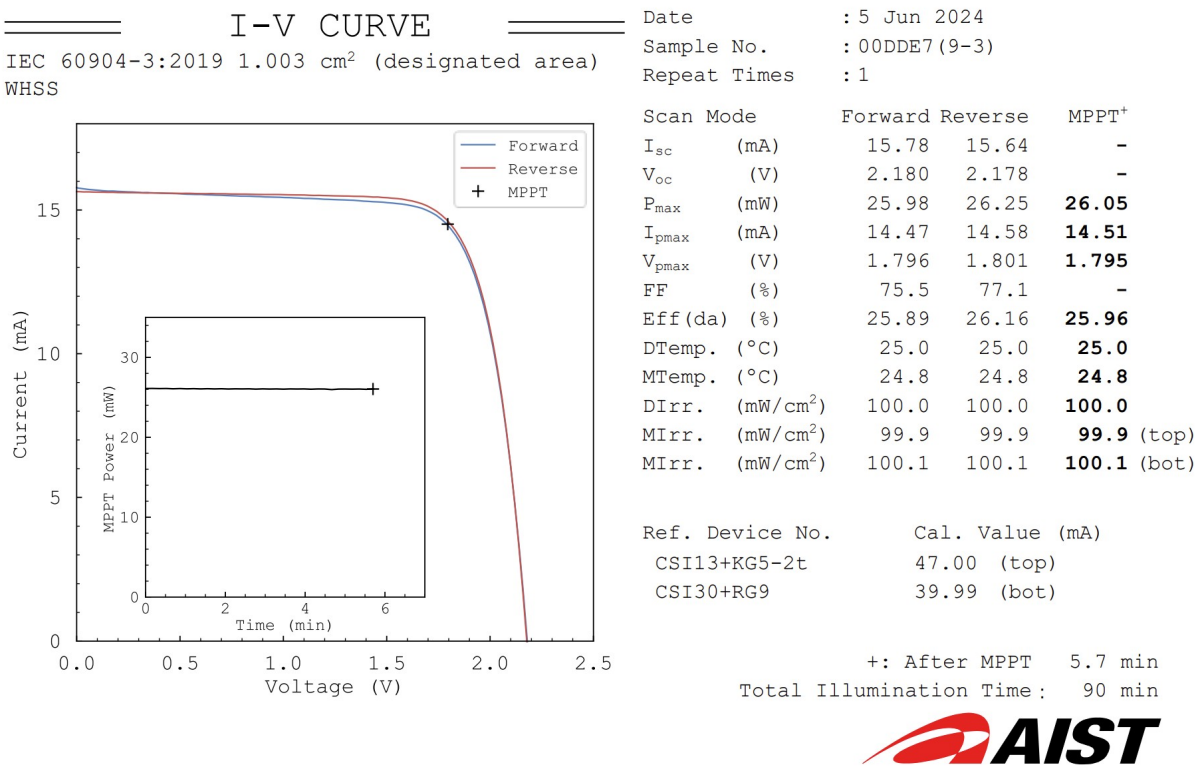

Supplementary Figure 26. Certified MPPT results (25.96%) from the National Institute of Advanced Industrial Science and Technology (AIST, Japan) of a 1 cm^2 double-junction cell.

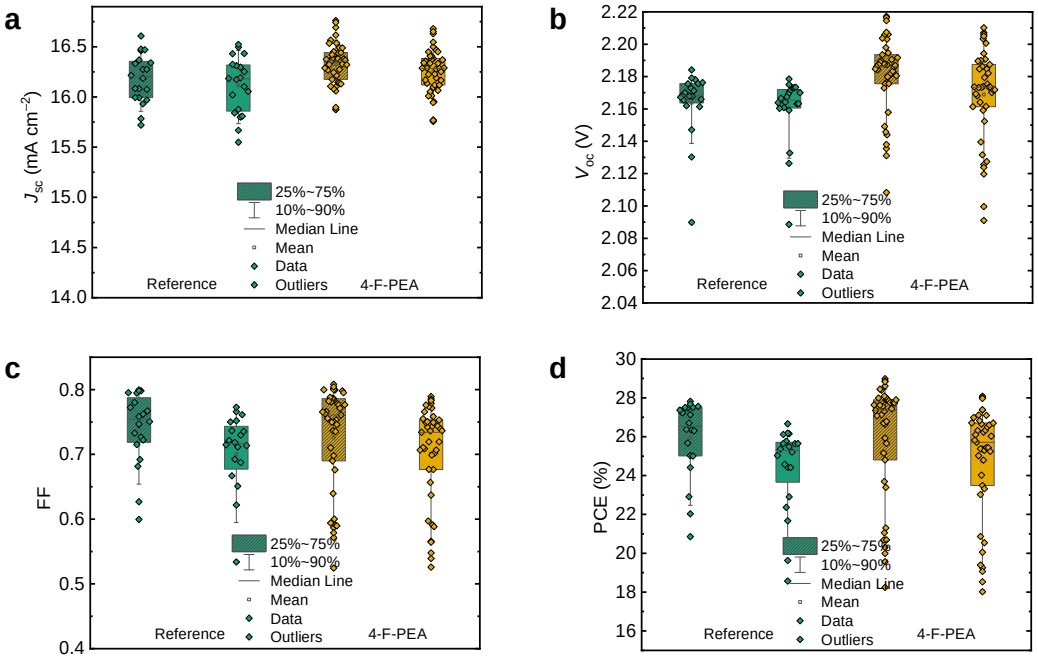

Supplementary Figure 27. Photovoltaic performance of all-perovskite tandem solar cells. PV parameters (reverse scans, left; forward scans, right) of reference and 4-F-PEA (1 mol%) devices. For each variation at least 20 devices from 2 different batches are shown. In the boxplots, the mean (open square), median (centre line), 25th and 75th percentiles (box limits), minimum (–) and maximum (+), outliers (△), and 10th and 90th percentiles (whiskers) are shown.

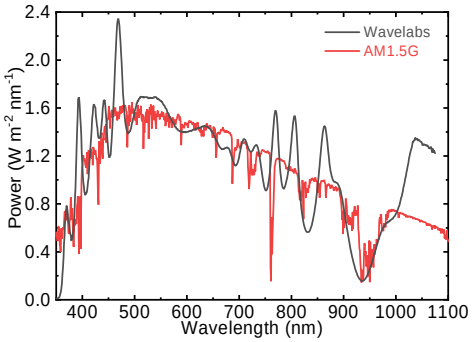

Supplementary Figure 28. Solar spectrum. AM1.5G and Wavelabs SINUS-220 simulator spectra[7]. The calculated mismatch factor for the current-limiting junction is 0.994.

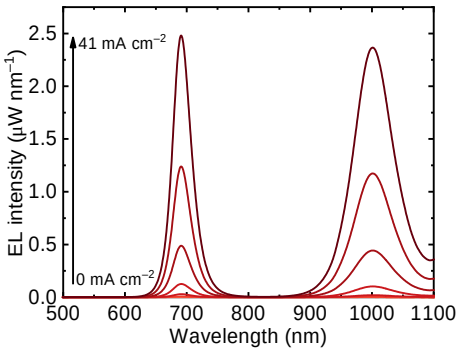

Supplementary Figure 29. Emission spectra of integrated tandem solar cells. Injection current-dependent EL spectra of tandem solar cells measured from 0 to 41 mA cm^{-2}.

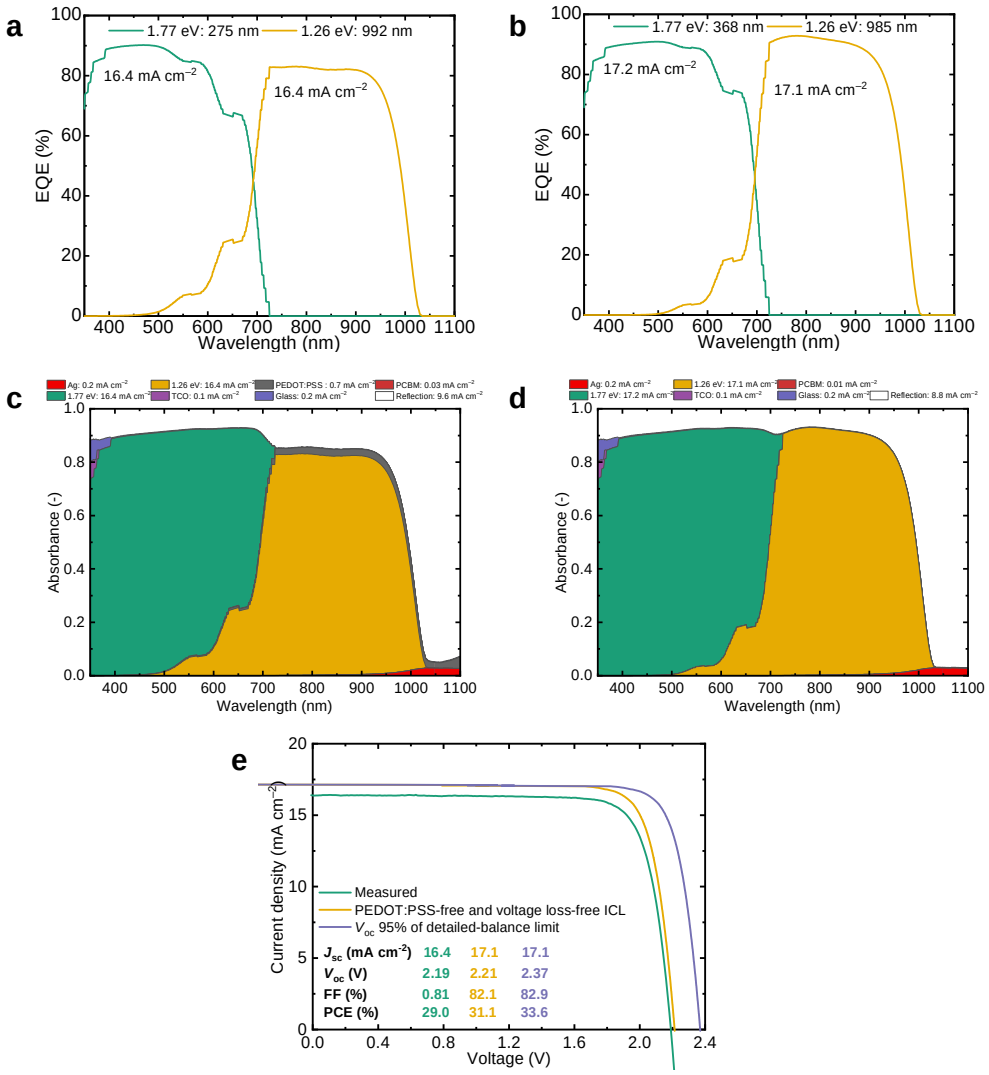

Supplementary Figure 30. Optical simulations. **a**,**c**, Simulated EQE (**a**) and absorption profiles (**c**) of tandem solar cells by decreasing the thickness of the 1.77 eV film from 365 to 275 nm and increasing the thickness of the 1.26 eV film from 840 to 992 nm. **b**,**d**, Simulated EQE (**b**) and absorption profiles (**d**) of tandem solar cells after eliminating the PEDOT:PSS HTL. Practical absorber layer thicknesses of 368 nm for the 1.77 eV perovskite and 985 nm for the 1.26 eV perovskite are used to obtain an EQE-integrated J_{SC} of ~17.1 mA cm^{-2}. **e**, Experimental and reconstructed *J*–*V* characteristics shifted to the simulated EQE-integrated currents (~17.1 mA cm^{-2}) and assumed a V_{OC} of 95% of the detailed-balance limit in each sub-cell. The sub-cells used to construct the tandem *J*–*V* are from the measured single-junction cell data.

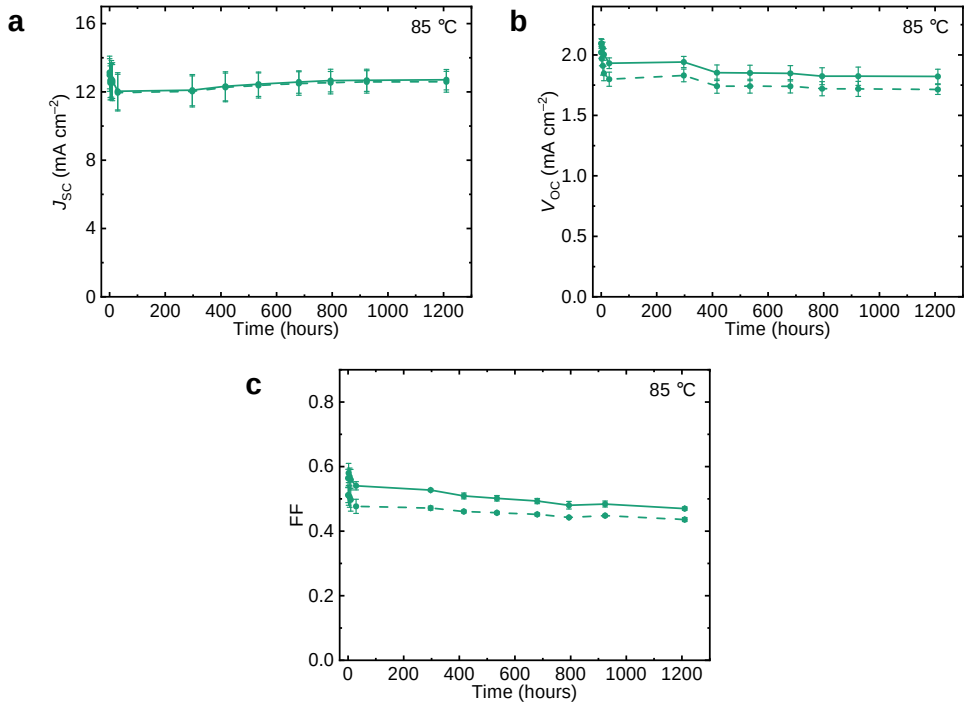

Supplementary Figure 31. Photovoltaic performance of all-perovskite tandem solar cells during ageing. The PV parameters of **a**, J_{SC}, **b**, V_{OC}, and **c**, FF of encapsulated solar cells measured after storing at 85 °C in the dark in N_2 (**Fig. 4e**). The solid lines are data points from reverse scans while the dashed lines are from the forward scans. Within the first 30 hours of ageing, we observe a decrease in the mean J_{SC} of 1.1 (1.0) mA cm^{-2}, a drop in the V_{OC} of 0.16 (0.22) V, and a reduction in the FF of 2 (3)% for reverse (forward) scans. The mean MPP efficiency decreased to 77%. This significant decay in all the parameters is attributed to poor charge extraction and degraded contact properties. We believe that further investigations into surface passivation materials capable of creating a strong binding affinity with the perovskite surface, such as the amino-silane molecules[8], may significantly enhance device stability under elevated temperature light-soaking ageing conditions.

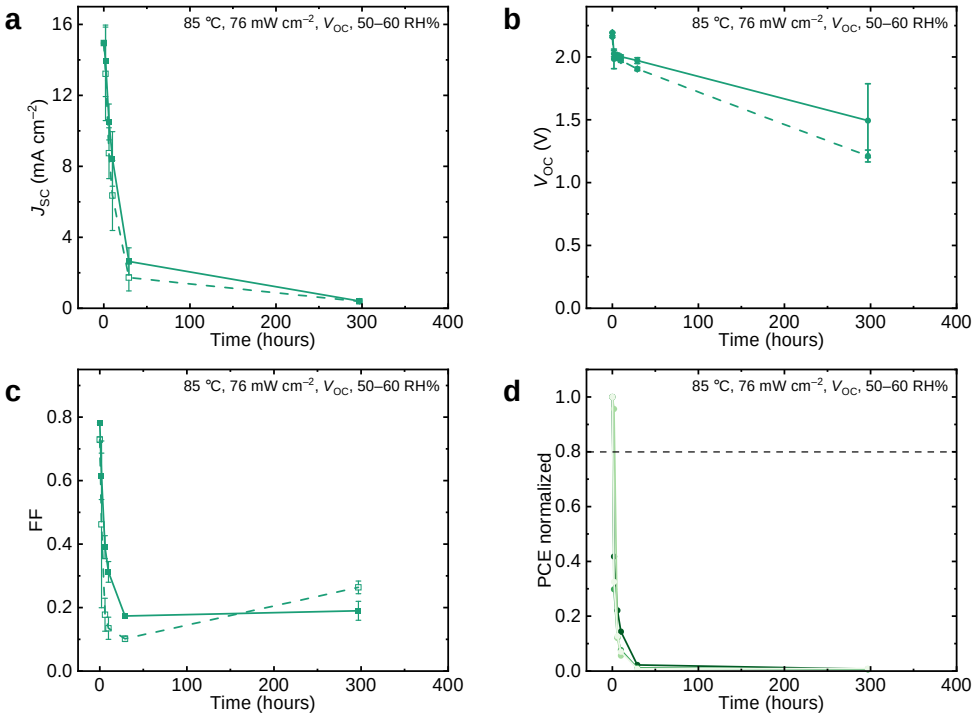

Supplementary Figure 32. Photovoltaic performance of all-perovskite tandem solar cells during ageing. The PV parameters of **a**, J_{SC}, **b**, V_{OC}, **c**, FF, and **d**, PCE (MPP efficiency) of encapsulated solar cells measured after storing at 85 °C in ambient under full-spectrum simulated sunlight (~76 mW cm^{-2}). The solid lines are data points from reverse scans while the dashed lines are from the forward scans. The RH is a measure of the room of the ageing box.

Supplementary Table 1. PEA cations. Dipole moment of PEA and FA cations.

Cation	Dipole moment (Debye)
pFPEA	12.43
mFPEA	11.25
oFPEA	8.89
PEA	9.42
FA	0.22

Supplementary Table 2. Film crystallinity. Fitted peak areas of (100), (110), and (111) planes and their summed values using 1D XRD from **Fig. 1e**.

Integrated area (a.u.)	(100)	(110)	(111)	Sum
Reference (0%)	89.7	143.7	35.6	269.0
4-F-PEA 1 mol%	223.5	143.5	33.1	400.1
4-F-PEA 2 mol%	256.4	121.5	32.7	410.6
4-F-PEA 5 mol%	309.6	106.6	35.2	451.4
4-F-PEA 10 mol%	360.4	104.5	36.5	501.4

References

1. E. Heifets, R. I. Eglitis, E. A. Kotomin, J. Maier and G. Borstel, Ab initio modeling of surface structure for $SrTiO_3$ perovskite crystals, *Phys. Rev. B*, 2001, **64**, 235417.
2. Y.-K. Jung, J.-H. Lee, A. Walsh and A. Soon, Influence of Rb/Cs Cation-Exchange on Inorganic Sn Halide Perovskites: From Chemical Structure to Physical Properties, *Chem. Mater.*, 2017, **29**, 3181–3188.
3. J. Hu, I. W. H. Oswald, S. J. Stuard, M. M. Nahid, N. Zhou, O. F. Williams, Z. Guo, L. Yan, H. Hu, Z. Chen, X. Xiao, Y. Lin, Z. Yang, J. Huang, A. M. Moran, H. Ade, J. R. Neilson and W. You, Synthetic control over orientational degeneracy of spacer cations enhances solar cell efficiency in two-dimensional perovskites, *Nat. Commun.*, 2019, **10**, 1276.
4. H. Guthrey and J. Moseley, A Review and Perspective on Cathodoluminescence Analysis of Halide Perovskites, *Adv. Energy Mater.*, 2020, **10**, 1903840.
5. W. H. M. Remmerswaal, B. T. van Gorkom, D. Zhang, M. M. Wienk and R. A. J. Janssen, Quantifying Non-Radiative Recombination in Passivated Wide-Bandgap Metal Halide Perovskites Using Absolute Photoluminescence Spectroscopy, *Adv. Energy Mater.*, 2024, **14**, 2303664.
6. T. J. Jacobsson, A. Hultqvist, A. García-Fernández, A. Anand, A. Al-Ashouri, A. Hagfeldt, A. Crovetto, A. Abate, A. G. Ricciardulli, A. Vijayan, A. Kulkarni, A. Y. Anderson, B. P. Darwich, B. Yang, B. L. Coles, C. A. R. Perini, C. Rehermann, D. Ramirez, D. Fairen-Jimenez, D. Di Girolamo, D. Jia, E. Avila, E. J. Juarez-Perez, F. Baumann, F. Mathies, G. S. A. González, G. Boschloo, G. Nasti, G. Paramasivam, G. Martínez-Denegri, H. Näsström, H. Michaels, H. Köbler, H. Wu, I. Benesperi, M. I. Dar, I. Bayrak Pehlivan, I. E. Gould, J. N. Vagott, J. Dagar, J. Kettle, J. Yang, J. Li, J. A. Smith, J. Pascual, J. J. Jerónimo-Rendón, J. F. Montoya, J.-P. Correa-Baena, J. Qiu, J. Wang, K. Sveinbjörnsson, K. Hirselandt, K. Dey, K. Frohna, L. Mathies, L. A. Castriotta, M. H. Aldamasy, M. Vasquez-Montoya, M. A. Ruiz-Preciado, M. A. Flatken, M. V. Khenkin, M. Grischek, M. Kedia, M. Saliba, M. Anaya, M. Veldhoen, N. Arora, O. Shargaieva, O. Maus, O. S. Game, O. Yudilevich, P. Fassl, Q. Zhou, R. Betancur, R. Munir, R. Patidar, S. D. Stranks, S. Alam, S. Kar, T. Unold, T. Abzieher, T. Edvinsson, T. W. David, U. W. Paetzold, W. Zia, W. Fu, W. Zuo, V. R. F. Schröder, W. Tress, X. Zhang, Y.-H. Chiang, Z. Iqbal, Z. Xie and E. Unger, An open-access database and analysis tool for perovskite solar cells based on the FAIR data principles, *Nat. Energy*, 2022, **7**, 107−115.
7. S. Hu, J. Wang, P. Zhao, J. Pascual, J. Wang, F. Rombach, A. Dasgupta, W. Liu, M. A. Truong, H. Zhu, M. Kober-Czerny, J. N. Drysdale, J. A. Smith, Z. Yuan, G. J. W. Aalbers, N. R. M. Schipper, J. Yao, K. Nakano, S.-H. Turren-Cruz, A. Dallmann, M. G. Christoforo, J. M. Ball, D. P. McMeekin, K.-A. Zaininger, Z. Liu, N. K. Noel, K. Tajima, W. Chen, M. Ehara, R. A. J. Janssen, A. Wakamiya and H. J. Snaith, Steering perovskite precursor solutions for multijunction photovoltaics, *Nature*, 2024, **639**, 93–101.
8. Y.-H. Lin, F. Yang, X.-L. Cao, A. Dasgupta, R. D. J. Oliver, A. M. Ulatowski, M. M. McCarthy, X. Shen, Q. Yuan, M. G. Christoforo, F. S. Y. Yeung, M. B. Johnston, N. K. Noel, L. M. Herz, M. S. Islam and H. J. Snaith, Bandgap-universal passivation enables stable perovskite solar cells with low photovoltage loss, *Science*, 2024, **384**, 767–775.